Simulation of a Stratocumulus-Topped Planetary Boundary Layer: Intercomparison among Different Numerical Codes

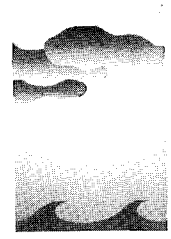

C.-H. Moeng,* W. R. Cotton,+ C. Bretherton,# A. Chlond,@ M. Khairoutdinov,&
S. Krueger,** W. S. Lewellen,++ M. K. MacVean,## J. R. M. Pasquier,@@ H. A. Rand,#
A. P. Siebesma,&& B. Stevens,+ and R. I. Sykes***

ABSTRACT

This paper reports an intercomparison study of a stratocumulus-topped planetary boundary layer (PBL) generated from ten 3D large eddy simulation (LES) codes and four 2D cloud-resolving models (CRMs). These models vary in the numerics, the parameterizations of the subgrid-scale (SGS) turbulence and condensation processes, and the calculation of longwave radiative cooling. Cloud-top radiative cooling is often the major source of buoyant production of turbulent kinetic energy in the stratocumulus-topped PBL. An idealized nocturnal stratocumulus case was selected for this study. It featured a statistically horizontally homogeneous and nearly solid cloud deck with no drizzle, no solar radiation, little wind shear, and little surface heating.

Results of the two-hour simulations showed that the overall cloud structure, including cloud-top height, cloud fraction, and the vertical distributions of many turbulence statistics, compared well among all LESs despite the code variations. However, the entrainment rate was found to differ significantly among the simulations. Among the model uncertainties due to numerics, SGS turbulence, SGS condensation, and radiation, none could be identified to explain such differences. Therefore, a follow-up study will focus on simulating the entrainment process. The liquid water mixing ratio profiles also varied significantly among the simulations; these profiles are sensitive to the algorithm used for computing the saturation mixing ratio.

Despite the obvious differences in eddy structure in two- and three-dimensional simulations, the cloud structure predicted by the 2D CRMs was similar to that obtained by the 3D LESs, even though the momentum fluxes, the vertical and horizontal velocity variances, and the turbulence kinetic energy profiles predicted by the 2D CRMs all differ significantly from those of the LESs.

*National Center for Atmospheric Research, Boulder, Colorado.
+Colorado State University, Fort Collins, Colorado.
#University of Washington, Seattle, Washington.
@Max-Planck-Institut für Meteorologie, Germany.
&University of Oklahoma, Norman, Oklahoma.
**University of Utah, Salt Lake City, Utah.
++West Virginia University, Morgantown, West Virginia.
##U.K. Meteorological Office, United Kingdom.
@@Institute of Science and Technology, University of Manchester, Manchester, United Kingdom.
&&KNMI, the Netherlands.
***Titan Research and Technology, New Jersey.
Corresponding author address: Dr. C.-H. Moeng, Mesoscale and Microscale Meteorology Division, National Center for Atmospheric Research, P.O. Box 3000, Boulder, CO 80307-3000.
E-mail: moeng@ncar.ucar.edu
In final form 28 July 1995.

1. Introduction

One of the main objectives of the Global Energy and Water Cycle Experiment Cloud System Study (GCSS) Program is to develop cloud parameterization schemes for use in climate models through the use of numerical data generated from large eddy simulations (LESs) or cloud resolving models (CRMs) (Browning 1993). Naturally, the first step is to examine the accuracy of these numerically generated data in representing cloud statistics in the context of developing or calibrating cloud parameterization schemes for climate models. Since there are very few complete observational datasets with which to evaluate the simulation performance, an alternative method to check the accuracy of the numerical database is to intercompare

simulation results from different numerical codes to see if results are sensitive to numerical schemes or parameterizations of certain physical processes as discussed in the following.

The fundamental approach of LES is to explicitly resolve large turbulent eddies, which contain most turbulent kinetic energy and do most transport; hence, an LES for the planetary boundary-layer turbulent motion should be three dimensional. In this paper, we refer to all 3D simulations as LESs and two-dimensional simulations as 2D CRM simulations.

Although LES explicitly resolves most important eddies, uncertainties still exist in those simulations. The effect of subgrid-scale turbulent motion (i.e., scales less than few tens of meters in a typical LES) is parameterized through a subgrid-scale (SGS) model, which leads to some uncertainty in small-scale mixing. This is particularly important near the ground and near cloud top, where the scales of turbulence are mostly SGS. There is always uncertainty due to numerics. Two earlier intercomparison studies of a pure buoyancy-driven clear planetary boundary layer (PBL) (Nieuwstadt et al. 1993) and a pure shear-driven clear PBL (Andren et al. 1994) found that the turbulence statistics produced from four different LES codes were quite comparable. Those studies suggested that the simulation results were not sensitive to the treatment of small-scale mixing and the numerical methods, at least for clear PBL turbulence simulations.

For cloudy PBL, other uncertainties arise from the fact that the effects of radiation and the SGS condensation/evaporation are both parameterized processes in LESs. For the stratocumulus-topped PBL, the former effect could be large because cloud-top radiation cooling is often the dominant source, via buoyancy production, for turbulent kinetic energy. The SGS condensation/evaporation process may also play an important role in generating or consuming turbulence. In addition, algorithms used in computing the saturation mixing ratio are different among different codes.

In 2D CRM simulations, additional uncertainty comes from the assumed two dimensionality of the turbulent flow. It is known that 2D flow fields do not allow vortex stretching, and hence, can be very different from those of 3D simulations. But given the same forcings, differences in the averaged turbulence statistics between 2D and 3D simulations may be less significant than differences in instantaneous flow realizations. Since there are advantages to performing 2D simulations, such as being able to use a finer grid, a much larger domain coverage, or a much longer time integration than 3D simulations can given the same computer resources, we would like to find out what statistics can/cannot be reasonably produced by 2D simulations.

To see how sensitive numerically generated data are to the above-mentioned uncertainties, to examine the feasibility of 2D CRM simulations, and also to provide a database for 1D boundary-layer cloud scheme development, the GCSS Boundary-Layer Cloud Working Group (chaired by W. R. Cotton) plans to carry out a series of intercomparison studies of simulations for various PBL cloud types using different LES and 2D CRM codes and at the same time to examine the performance of different one-dimensional parameterization schemes.

The first of these studies took place at the National Center for Atmospheric Research (NCAR)/GCSS Boundary Layer Cloud Workshop on 16–18 August 1994. Ten LES and four 2D CRM groups from the United States and western Europe (described in section 2) participated in this intercomparison study. The simulation case selected for this study is described in section 3. The 3D and 2D results are reported and compared in section 4, while discussion and future work are presented in section 5.

Six 1D cloud modeling groups also participated in the intercomparison. The 1D models are ensemble mean turbulence closure schemes that were developed as cloud parameterization schemes for large-scale meteorological forecast or climate models. The six models include a two-layer bulk model presented by S. Wang, a 1.5-order closure scheme by P. Bechtold, the Second-Order Bulk Model by D. Randall, a single-column K-profile-type model by A. van Ulden, a simplified second-order closure scheme by S. Lewellen, and a third-order closure scheme by S. Krueger and Q. Shao. Results from these models were quite varied, with some of the models yielding results that are comparable to the statistics from the 2D or 3D simulations. Since some of these models are still in the developmental stage, we have chosen not to report any results from them in this paper.

2. Descriptions of the LES and CRM codes

a. The 3D LES codes

1) Numerics

The LES groups, the scientists who worked on this particular project, the velocity and scalar advection schemes used, the time integration schemes adopted,

and the time step used are listed in Table 1, where FD is finite differencing and AB is the Adams–Bashforth scheme. The institutions that these groups represent and a reference that describes each code are listed in appendix A. Most of these codes were developed independently, except that the University of Manchester Institute of Science and Technology (UMIST) LES originated from the U.K. Meteorological Office (UKMO) but uses different cloud microphysical and IR radiation schemes; the University of Oklahoma (UOK) LES has the same physics schemes as the NCAR LES but uses a totally different numerical method; and the Aeronautical Research Associates of Princeton, Inc. (ARAP) LES and the West Virginia University (WVU) LES are basically the same code but run independently.

TABLE 1. The large eddy simulation codes: scientists and numerics.

LES	Scientist	Advection	Time scheme	Time step (s)
KNMI	P. Siebesma	2d-order FD	Leapfrog	4
UKMO	M. MacVean	2d and 3d FD	Leapfrog	~0.46
UMIST	J. Pasquier	2d and 3d FD	Leapfrog	0.6
UW	H. Rand	2d-order FD	Leapfrog	5
MPI	A. Chlond	2d and Bott FD	AB 2d	2
NCAR	C.-H. Moeng	mixed spectral–FD	AB 2d	0.5
UOK	M. Khairoutdinov	5th-order FD in x, y	AB 3d	2
ARAP	I. Sykes	2d-order FD	Leapfrog	~2
WVU	S. Lewellen	2d-order FD	Leapfrog	~2
CSU	B. Stevens	6th-order FD	Leapfrog	2

The spatial representations vary from higher-order finite differencing to spectral representation. The time integration schemes are mainly leapfrog and Adams–Bashforth; among those using the leapfrog scheme, the smoothing schemes used to prevent time splitting also vary. The numerical time steps used vary as well, ranging from ~0.5 to 5 s.

2) SUBGRID-SCALE TURBULENCE PHYSICS

In an LES, large turbulent eddies that contain most of the kinetic energy are explicitly calculated, while those smaller than the effective grid mesh size are parameterized. Ideally, the SGS eddies in an LES grid mesh should lie within the inertial subrange, where the energy spectrum to some degree of approximation reaches a quasi-equilibrium state and remains at a $-5/3$ slope. In the statistical sense, the inertial subrange eddies are passive; they simply transfer energy cascaded from large eddies to dissipative eddies in a statistical equilibrium. Thus, in principle, LES results should not be too sensitive to the parameterization of the SGS eddies. (However, near the earth's surface and in the inversion layer above the PBL top where all eddies are small, LES solution is sensitive to the SGS parameterization.)

About one half of the LES codes used the SGS model developed by Smagorinsky (1963) and later elaborated by Lilly (1967), as shown in Table 2. This type of SGS model assumes that the shear and buoyancy productions in the SGS turbulent kinetic energy (TKE) budget balance the molecular dissipation locally. The resulting eddy viscosity or diffusivity is proportional to the local velocity and temperature gradients. However, the proportionality constant in the eddy viscosity formula, that is, the so-called Smagorinsky constant, may be quite different among the codes; some models relate the magnitude of this constant to the effective grid resolution (Mason and Callen 1986), while others relate it to the inertial subrange spectral slope (Lilly 1967).

The other half of the LESs, such as those of the Royal Netherlands Meteorological Institute (KNMI), the Max-Plank-Institute für Meteorologie (MPI), NCAR, and UOK, solved the SGS TKE equation proposed by Deardorff (1980a). This TKE equation SGS model is, in principle, similar to the Smagorinsky–Lilly diagnostic SGS model because the local production–dissipation balance approximately holds for the small eddies. Carrying an extra prognostic equation in LES does not add much computational burden since most of the computation is in calculating the shear production term, which is required in both types of SGS models. Solving the SGS TKE equation, however, does provide better insights into the SGS physics aspect, as discussed in Moeng and Wyngaard (1988), and the SGS TKE field is readily available, which makes diagnostics easier.

The ARAP/WVU model has somewhat different SGS physics. It also uses the SGS TKE equation but does not necessarily tie the unresolved turbulent length directly to the grid mesh. This turbulent length scale can be specified so that the SGS turbulence model acts as a turbulent closure model to predict ensemble mean statistics. When the grid mesh is smaller than the turbulent energy containing eddies, that is, very much smaller than 1 km, as in this exercise, the turbulent length scale is tied to the grid mesh, and the SGS model parameterizes just the part of turbulent eddies that is smaller than the effective grid mesh. This provides a general numerical code for including SGS turbulence.

The surface flux formulas may also differ among the LES codes. However, since the particular stratocumulus-topped PBL we chose to simulate had little surface heat flux, variations in computations of the surface flux should not have affected the results significantly.

3) SUBGRID-SCALE CONDENSATION/EVAPORATION

Table 2 lists the SGS condensation/evaporation schemes that these LES groups used. There are three types. 1) The 0% or 100% scheme assumes that within each grid box the air is either entirely unsaturated or entirely saturated. No partial cloud cover is allowed within each grid box, and no supersaturation is considered. 2) A subgrid-scale condensation scheme, developed by Sommeria and Deardorff (1977; denoted as the S–D SGS scheme hereafter), allows for the dependence of partial cloud cover on the SGS variances and covariance of the temperature and moisture fields. 3) An explicit (or bin) microphysics scheme, as used in the Colorado State University (CSU) LES, carries equations of a spectrum of droplets and allows for drizzle formation. However, for this intercomparison study, which is a no-drizzle case, the CSU explicit microphysics scheme is basically the same as the 0% or 100% scheme.

4) LONGWAVE RADIATION SCHEME

In this study, we included only longwave radiation (referred to as IR), which is parameterized in a simple emissivity approach by all LESs, also listed in Table 2. Solar radiation is excluded for this nighttime stratus simulation. Some LES codes calculated just the liquid water emissivity in their longwave radiation schemes, while the others calculated both vapor and liquid emissivities. All used a greybody emission assumption for cloud emissivity.

Even with the simple emissivity approach, computing the radiation field is more costly than computing the dynamical flow field. Thus, several LES groups calculated the longwave radiation at a time interval that is coarser than that used for dynamics calculation. Those groups include KNMI, which computed the radiation field every 2 min; University of Washington (UW), every ~5 min; UMIST, every 6 s; and CSU, every 10 s. Between each radiation calculation step, the radiation heating rate at each grid point was held constant.

Different treatments of the upper-boundary condition for the radiation calculation may also contribute to the variations of cloud-top IR cooling. Some codes prescribed a downward radiation flux at the top of the numerical domain, while the others prescribed a fixed amount of water vapor path above the top of the numerical domain. This gives

TABLE 2. The SGS turbulence, condensation, and longwave radiation schemes used in the LES codes.

LES	SGS turbulence	SGS condensation	IR scheme
KNMI	Deardorff TKE Eq.	0% or 100%	Stephens and Welch et al.
UKMO	Smagorinsky–Lilly	0% or 100%	greybody, q_l only
UMIST	Smagorinsky–Lilly	0% or 100%	mixed emissivity
UW	Smagorinsky–Lilly	0% or 100%	Roach–Slingo, q_l only
MPI	Deardorff TKE Eq.	S–D SGS condensation	Cox–Stephens, q_l only
NCAR	Deardorff TKE Eq.	0% or 100%	mixed emissivity
UOK	Deardorff TKE Eq.	0% or 100%	mixed emissivity
ARAP	ARAP TKE Eq.	S–D SGS condensation	greybody, q_l only
WVU	ARAP TKE Eq.	S–D SGS condensation	greybody, q_l only
CSU	Smagorinsky–Lilly	explicit microphysics	mixed emissivity

a different amount of the downward flux at the cloud top, and thus, the cloud-top IR cooling is different.

b. The 2D CRM codes

Four 2D CRM results were submitted for this intercomparison study from the University of Washington, the Colorado State University, the UKMO, and the University of Utah. They are labeled as UW-2D, CSU-2D, UKMO-2D, and UU-2D, respectively (also shown in appendix A). The UW-2D, CSU-2D, and UKMO-2D codes have the same numerics, SGS turbulence, and condensation schemes as their 3D counterparts, which were given in Tables 1 and 2. The only difference between their 3D and 2D codes is the assumption of two dimensionality in the latter by setting the flow field in one of the horizontal directions as uniform.

The UKMO-2D CRM orients its coordinate system such that the geostrophic wind direction is along the assumed uniform flow direction. The rationale behind this orientation is as follows. If quasi-2D roll-type motions dominate, they tend to be aligned closely to the wind direction. So the natural choice for a 2D numerical domain is to be perpendicular to the geostrophic wind. The other three 2D CRMs, however, just choose the north–south coordinate to be the uniform flow direction.

The UU-2D CRM, described in Krueger et al. (1995), uses an ensemble mean, third-moment turbulence closure for the SGS effects. The turbulent length scale is related to the scale of the parameterized small-scale turbulent eddies, not to the grid size. Thus, all 3D turbulent eddies are unresolved motions. The SGS condensation scheme is basically of the Sommeria–Deardorff type, which assumes that the subgrid-scale turbulent fluctuations of the conserved variables (liquid water static energy and total water mixing ratio) have a Gaussian distribution. The fluctuation statistics (i.e., variances and covariances) are predicted from the ensemble mean turbulence closure scheme. The IR radiative transfer code, developed by Fu (see Krueger et al. 1995), uses the correlated k-distribution approach and the delta-four stream method.

3. An idealized nighttime stratocumulus case

For this first intercomparison study, we chose an idealized nighttime stratocumulus-topped PBL case, that is, one that was horizontally homogeneous, had nearly solid cloud deck, no drizzle, no solar radiation, little wind shear, and little surface heating. This cloudy PBL was driven mainly by cloud-top radiation cooling and modified by the entrainment and condensation/evaporation processes.

Solar radiative heating inside the cloud layer can greatly complicate the turbulent structure. In addition, there is no proper solar radiation scheme for use in LES. Therefore, we chose to exclude solar radiative heating for our first intercomparison study.

Few stratocumulus observations were taken at night. Thus, we designed our large-scale and initial conditions to be based loosely on the FIRE [First ISCCP (International Satellite Cloud Climatology Project) Regional Experiment] 7 July 1987 uniform solid cloud case reported in Betts and Boers (1990) and in Duda et al. (1991). To facilitate the analysis, a series of simplifications was made to the observed case: 1) the sounding was smoothed to a piecewise linear format; 2) wind was slowed down to allow for a larger integration time step; and 3) only IR radiation was included to represent a nighttime simulation.

The sea surface temperature is 288 K, which gives a saturation mixing ratio of 10.67 g kg^{-1} and a virtual temperature of 289.85 K, assuming the sea level pressure is 1000 mb. The Coriolis parameter is set to 10^{-4} s^{-1}; large-scale divergence is 5×10^{-6} s^{-1}; the roughness length is 0.0002 m; the latent heat coefficient is 2.45×10^{6} J kg^{-1}; the specific heat of air is 1000 J K^{-1} kg^{-1}; air density is 1 kg m^{-3}; and the von Kármán constant set to 0.4. The geostrophic wind was set to be 2 m s^{-1} in the x (east–west) direction and -4 m s^{-1} in the y (north–south) direction.

a. Numerical setup

The grid size is about 55 m in x and y and about 25 m in z, covering a total numerical domain of 3–3.5 km in the horizontal directions and 1.2 km in the vertical. The numerical time step varies among the LESs, as shown in Table 1.

Some models used a varying grid in the vertical direction, which has a finer resolution near the surface and in the neighborhood of the inversion, while others used a uniform grid.

b. Initial sounding

The initial wind field was set to equal to the geostrophic wind, which, as mentioned, was smaller than the observation, reducing the effects of shear. The initial dry potential temperature θ and total moisture q_T profiles are given in Figs. 1a,b; the mathematical

description of this sounding is given in appendix B. Note that the initial dry potential temperature is nearly uniform in height, so the initial state is statically unstable within the cloud layer. Depending on the vertical grid setup (uniform or varying grid), the initial cloud-top height varied from 662.5 to 690 m. An initial SGS kinetic energy of 1 $m^2 s^{-2}$ was also specified at the levels below the initial cloud-top height for simulations including a TKE equation.

A random wind field with an amplitude of 0.5 m s^{-1} was imposed at the lowest four grid levels and a random temperature field with an amplitude of 0.1 K was given at the lowest level.

From the given dry potential temperature and total moisture fields, each LES model calculated its own initial liquid water content, and these are given in Fig. 1c. Notice that at the initial time, the liquid water mixing ratio already varied, ranging from ~0.4 to ~0.7 g kg^{-1}, with UW and WVU (also ARAP although its data are not available for the plot) diagnosing the most liquid water amount. This difference is mainly due to the different algorithms used to compute the saturation mixing ratio. Table 3 shows the saturation mixing ratio estimated by each LES group for θ = 288.32 K and z = 690 m. The UW, WVU, and ARAP produced the smallest amounts of saturation mixing ratio, ~7.37 g kg^{-1}, which is about 2% smaller than the rest. (The slight underestimate of the saturation mixing ratio in WVU/ARAP is due to their slight underestimate of the pressure and, thus, the absolute temperature rather than their saturation mixing ratio algorithms.) The initial liquid water fields of these three LES groups, therefore, had a peak value of about 0.7 g kg^{-1}, which is ~25% larger than the others. A larger initial liquid water field likely produces a larger initial radiative forcing at the cloud top.

TABLE 3. Calculated temperature, pressure, and saturation mixing ratio for a given reference state from the LES codes.

LES/CRM	Absolute temperature (K)	Pressure (mb)	Saturation mixing ratio (g kg^{-1})
KNMI	281.6	920.9	7.55
UKMO	281.5	920.8	7.54
UMIST	281.6	920.5	7.45
UW	281.6	920.6	7.38
MPI	281.7	921.4	7.53
NCAR	281.6	920.7	7.53
UOK	281.6	920.7	7.53
ARAP	281.3	917.4	7.37
WVU	281.3	917.4	7.37
CSU	281.6	920.8	7.56

From Fig. 1 we see that the dry potential temperature jump across the cloud top is about 6 K, while the

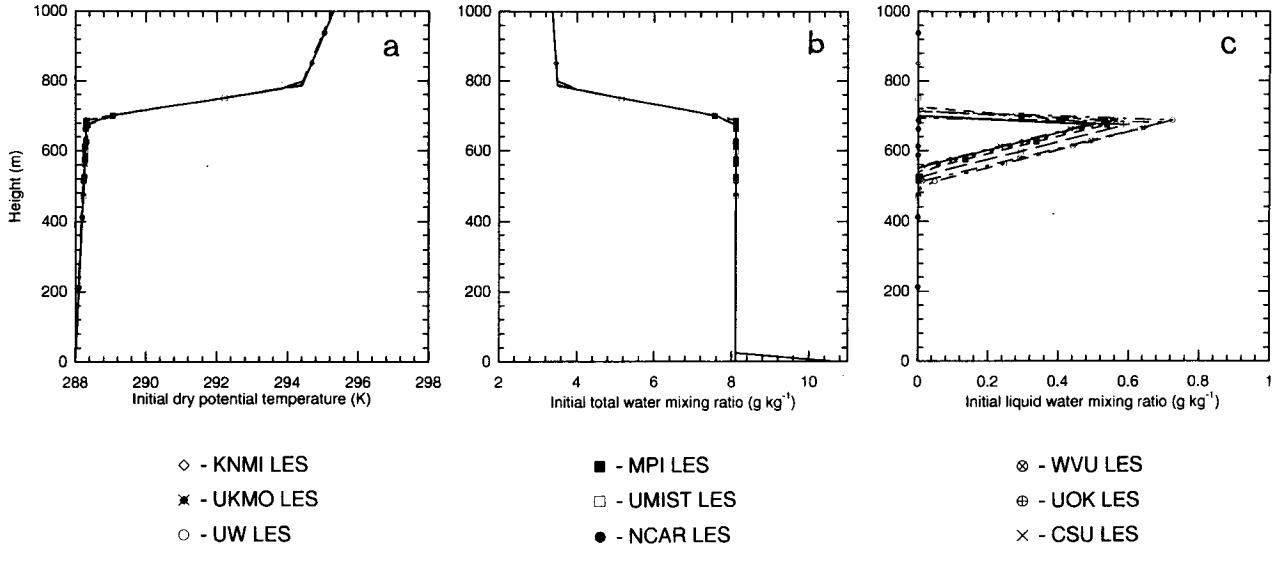

FIG. 1. Vertical profiles of the initial condition: (a) dry potential temperature, (b) total water mixing ratio, and (c) liquid water mixing ratio.

moisture jump is about -4.6 g kg^{-1}. This corresponds to an equivalent potential temperature jump of about -5.3 K. Thus, this cloud case is unstable with respect to the Randall–Deardorff cloud-top entrainment instability criterion (Randall 1980; Deardorff 1980b). However, the simulated cloud layer remains nearly solid as shown in section 4a(1), which agrees with the many other observations shown in Kuo and Schubert (1988) and also the criteria of MacVean and Mason (1990) and Siems et al. (1990) in similar regions of parameter space.

c. Observed quantities

For the 7 July stratocumulus cloud case, a near-zero surface sensible flux and a near 60 W m^{-2} surface latent heat flux were observed by Betts and Boers (1990), while a peak value in the liquid water content of 0.14 g m^{-3} was reported by Duda et al. (1991).

However, as we mentioned, we have smoothed the observed sounding, slowed the observed wind, and also turned off the solar radiation effect. These modifications and simplifications obviated the usefulness of comparing our simulations to observations.

4. Intercomparison results

a. The 3D LES results

It is important to note that the turbulence we simulated within the stratocumulus-topped PBL was driven mainly by longwave cooling at the cloud top. This major buoyancy forcing was internally determined, and unfortunately, it varied significantly between the various simulations.

Figure 2 shows the vertical distributions of the IR heating rates from the 10 LESs averaged over the second hour of the simulation. The maximum IR cooling at the cloud top varied from -3 to -6 K h^{-1}. KNMI and UW (open diamond and open circle) produced the largest cloud-top cooling (more than 5 K h^{-1}). As we will see later, these two LES runs produced the largest buoyancy flux within the cloud layer.

1) Time evolution

The time evolution of the mean cloud-top height, cloud cover, liquid water path (LWP), and vertically integrated turbulent kinetic energy of all 10 LESs is shown in Fig. 3. At the initial time, no resolved-scale turbulence existed except for the small random perturbations imposed near the surface. During the first 20–30 min, the simulations were in a spinup period; that is, the resolved-scale turbulence was not yet established. During this time period, the cloud top (Fig. 3a) did not grow much in most of the simulations since there was only SGS turbulence to induce entrainment. What happened during this time period is the following. With the initially uniform cloud layer, longwave radiative cooling occurred near the cloud top. This cooling resulted in an increasingly unstable lapse rate near the cloud top. When that thin near-cloud-top layer became very unstable, convective overturning suddenly took place, which initiated the resolved-scale turbulent motion. (This spinup process was different in the WVU/ARAP simulations; their cloud layers grew from the very beginning, probably because of the inclusion of effects of the cloud-top instability in their SGS turbulence.)

Toward the end of the 2-h simulation, the horizontally averaged cloud-top height z_i varied between 730 and 810 m. (Notice that at the initial time, the cloud-top heights were already different by up to 25 m, which is due to the different setup of the vertical grid levels.) The growth rate of the cloud-top height, which is the entrainment rate plus the given synoptic-scale vertical motion due to the specified large-scale divergence field, is quite different among the LESs, as shown in Table 4. Here, the cloud-top growth rate was computed as the averaged dz_i/dt over the second hour of the simulation period. KNMI and UOK gave the largest entrainment rates of all, while ARAP and

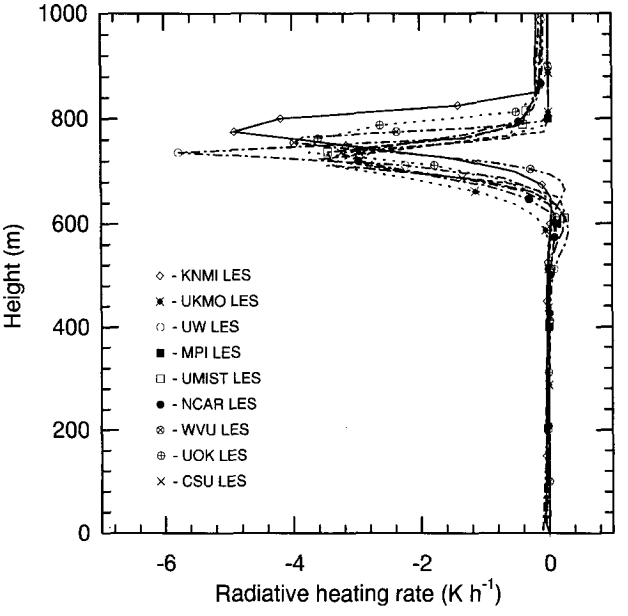

FIG. 2. Vertical profiles of the longwave radiative heating rate averaged over the second hour of simulation.

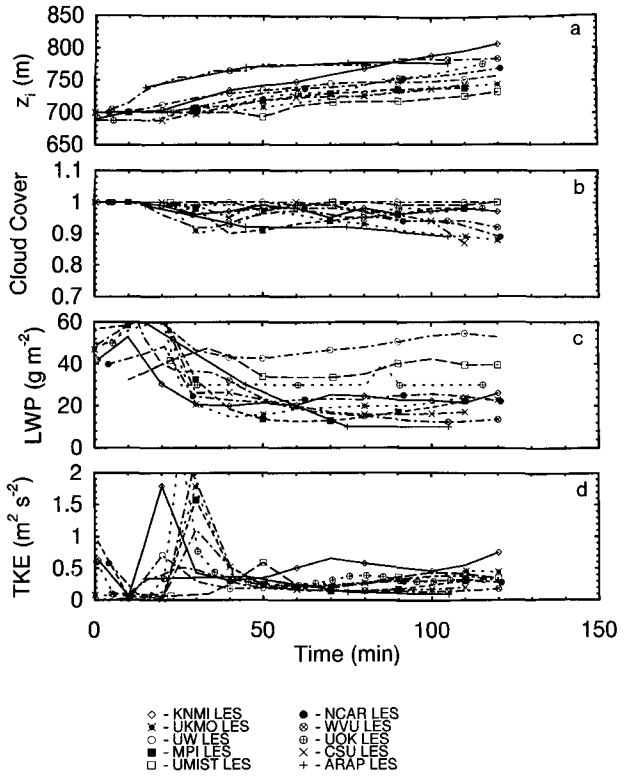

FIG. 3. Time evolution of (a) horizontally averaged cloud-top height, (b) fractional cloud cover, (c) liquid water path, and (d) TKE averaged over the whole PBL from the 10 LES simulations.

WVU gave the smallest. The difference between the largest and the smallest is a factor of 7! (The growth rate in the ARAP and WVU simulations was greater than the others during the initial stage but then became much less than the others during the second hour of the simulation period.)

The differences in the entrainment rates could be due to the different treatments of numerics, SGS turbulence, radiation, and/or SGS condensation. For example, a stronger cloud-top IR cooling could result in a stronger buoyancy forcing and, hence, larger TKE. Larger TKE is likely to induce a larger entrainment rate. However, the cloud-top IR cooling does not seem to be the only reason for such differences. As we compared Fig. 2 and Fig. 3, it became apparent that the physical treatments among all LES codes are too varied to allow us to evaluate the entrainment rate predictions. Therefore, during the workshop, we proposed an immediate follow-up study of a smoke cloud (i.e., dry dust cloud) simulation to study the entrainment rate, as described in section 5.

All LESs produced a nearly solid cloud cover that varied between 100% and 90%, as shown in Fig. 3b, with UMIST and UW simulations having about 100% cloud cover. The nearly solid cloud amount agrees with the nearly solid stratocumulus cloud observed during the 7 July FIRE even though the model sounding was modified somewhat.

The liquid water path (LWP) shown in Fig. 3c was calculated by vertically integrating the liquid water content, using an air density of 1 kg m^{-3}. It varied significantly, between 10 and 55 g m^{-2}, with UW having the largest and UMIST the second largest. Comparing Figs. 2 and 3c, we found no correlation between the predicted LWP and the cloud-top cooling amount, except for the UW result.

The TKE vertically averaged over the whole PBL is shown in Fig. 3d. Toward the end of the spinup time, a peak value in TKE occurred due to the above-mentioned convective overturning in most LESs. After about a 1-h simulation time, turbulence reached a quasi-steady state, in which the layer-averaged TKE remained nearly constant for each LES. (The total TKE values were different at the initial time for the following reason. The LES codes that used the Smagorinsky–Lilly-type SGS turbulence model required no explicit SGS energy to start up their runs, and therefore, their total initial TKE was zero except for the small random perturbation applied to the wind field at the lowest four grid levels. Others that solved the SGS TKE equation prescribed a 1 m^2 s^{-2} value at the initial time and, hence, had a layer-averaged TKE of that amount.)

TABLE 4. The averaged growth rate of the cloud-top height during the second hour of simulation.

LES	Averaged dz_i/dt (cm s^{-1})
KNMI	1.68
UOK	1.37
UMIST	0.94
NCAR	0.906
UKMO	0.856
CSU	0.686
UW	0.512
MPI	0.441
WVU	0.278
ARAP	0.236

Figure 4 shows scatter plots of (a) LWP versus cloud cover and (b) LWP versus layer-averaged TKE over the second hour of simulation. The predicted LWP amount is not well correlated with either the cloud cover or the layer-averaged TKE.

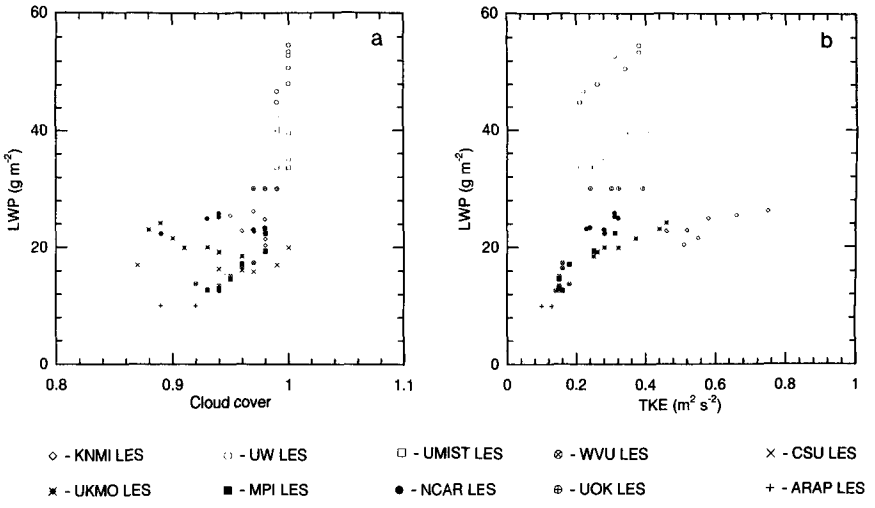

FIG. 4. Correlation plots of (a) fractional cloud cover vs liquid water path and (b) layer-averaged TKE vs liquid water path from the 10 LES simulations.

2) VERTICAL DISTRIBUTIONS OF THE MEANS AND FLUXES

The profiles of turbulence statistics described below were obtained by performing first a spatial average over the x–y planes and then a time average over the second hour of simulation, when turbulence was already well established and had reached a quasi-steady state for most LESs.

The mean wind (not shown), virtual potential temperature (Fig. 5a), and total water fields (Fig. 5b) look quite similar among the 10 LESs, although the difference in the total water mixing ratio within the cloud layer is close to 0.4 g kg^{-1}. This difference explains part of the variation in the peak value of the liquid water mixing ratio (Fig. 5c), which ranges from 0.1 to 0.35 g kg^{-1}. The three largest liquid water values were predicted by UW, UMIST, and UOK, in descending order, and the smallest amounts by ARAP and WVU. This variation is consistent with that in LWP. WVU and ARAP predicted the smallest amount of liquid water mixing ratio because their cloud layers entrained rapidly at the beginning of the simulation and, hence, evaporated more. Another reason for the varying liquid water mixing ratio is the different algorithms used in calculating the saturation mixing ratio, as we mentioned in section 3b. For example, the UW model consistently provided the largest liquid water mixing ratio near the cloud top, even at the initial time as shown in Fig. 1c.

The agreement on second-moment statistics is not as good as for the mean fields, as was expected. Figure 6a shows both total u-momentum flux (curves with a negative surface flux) and v-momentum flux (curves with a positive surface flux). Overall, the surface

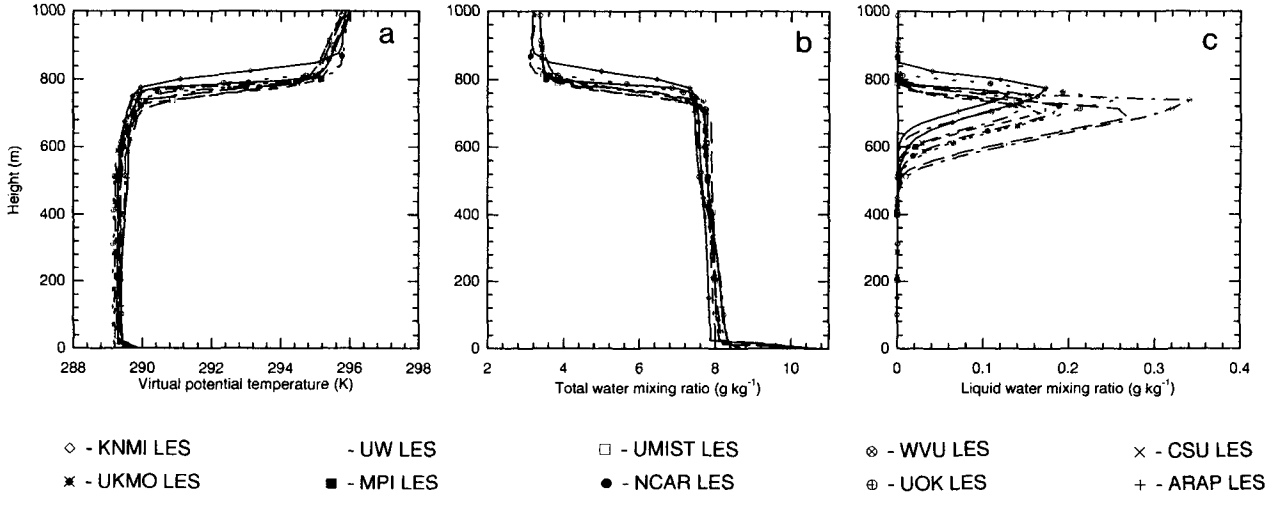

FIG. 5. Vertical profiles of (a) virtual potential temperature, (b) total water mixing ratio, and (c) liquid water mixing ratio averaged over the second hour of simulation from the 10 LES codes.

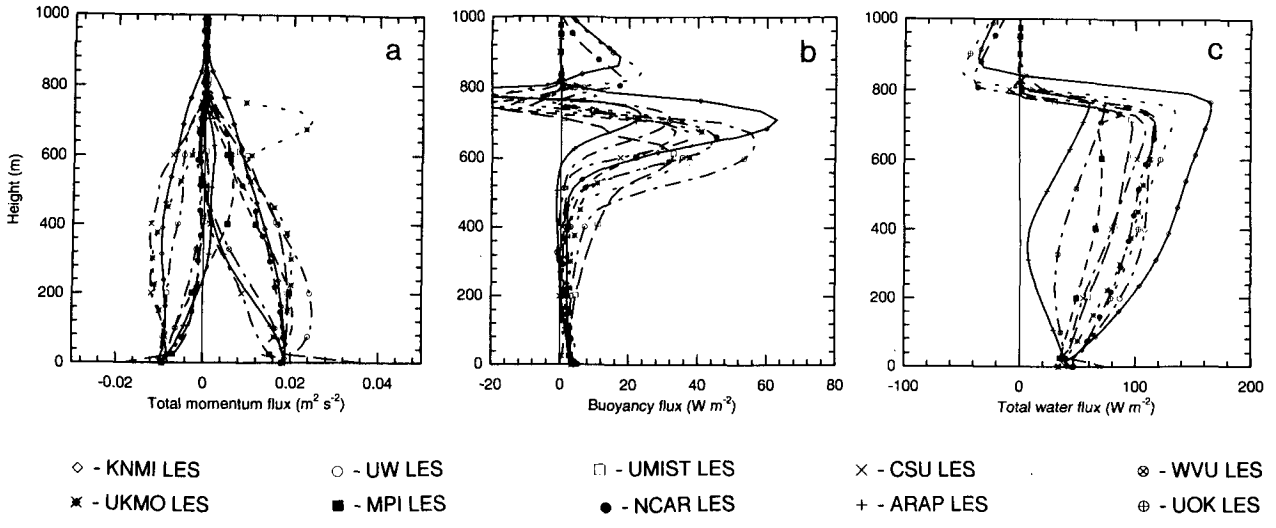

FIG. 6. Vertical profiles of (a) momentum fluxes of u and v, (b) buoyancy flux, and (c) total water flux averaged over the second hour of simulation from the 10 LES codes.

fluxes agree well among all simulations. In addition, both fluxes become zero just above the PBL, as expected. However, in between, the shapes of the flux profiles differ significantly. The scatter among the curves may be partially explained by the data sampling problem; it is known that a large amount of data is required to get statistically meaningful momentum fluxes (e.g., Lenschow and Stankov 1986).

Figure 6b presents the vertical distribution of the total buoyancy flux (resolved plus subgrid scale). Although it varied significantly in magnitude, the shape of this flux profile is similar among all LESs. All predicted a nearly zero buoyancy flux in the subcloud layer and a sudden increase near the cloud base. Notice that the largest buoyancy flux in the cloud layer was predicted by the KNMI and UW LESs, which is consistent with their larger cloud-top radiative cooling, shown in Fig. 2.

Figure 6c shows the total water flux (resolved plus subgrid-scale), which varied greatly among the LESs. The largest flux was predicted by KNMI and UOK, while the smallest total water flux was given by the ARAP, WVU, and MPI models. It is obvious that this variation is closely related to the entrainment rate prediction shown in Table 4. When turbulence reaches a statistically quasi-steady state, we expect to see a nearly linear profile of the total water flux (for a case without drizzle.) So, with about the same surface flux predicted by almost all LESs, a small entrainment rate would result in a smaller entrainment flux (which is the positive flux right beneath the cloud-top level), based on the jump model, $\overline{wq_{Ti}} = -w_e \Delta Q_T$, where $\overline{wq_{Ti}}$ is the total water entrainment flux, w_e is the entrainment rate, and ΔQ_T is the jump of the mean total water across the cloud top. Smaller entrainment flux means smaller total water flux everywhere within the PBL because of the linear-in-height distribution.

The nonlinear distributions produced by the ARAP, WVU, and MPI suggested that these simulations have not reached a statistically quasi-steady state; they need a time record of longer than one hour to achieve quasi-steady state statistics for this particular run. It is also interesting to note that the smallest entrainment rates (and, hence, smallest water flux) were simulated by the ARAP, WVU, and MPI models, which happen to use the S–D SGS condensation scheme.

The positive buoyancy flux, negative total water flux, and the low values of total water mixing ratio above the cloud top (above ~800 m) predicted by NCAR, UOK, and KNMI are numerically spurious; they are due to the use of centered finite differencing for vertical advection of scalar field across a sharp gradient zone. This numerical problem can be avoided by adopting a monotonic advection scheme.

3) VERTICAL PROFILES OF THE TKE AND ITS BUDGETS

The total (resolved plus subgrid-scale) TKE profiles (Fig. 7a; the KNMI and ARAP results are unavailable) varied greatly, for example, from about 0.1 $m^2 s^{-2}$ to about 0.3 $m^2 s^{-2}$ in the mid-PBL. This TKE variation appeared in both the resolved-scale horizontal ($\overline{u^2} + \overline{v^2}$) and vertical components ($\overline{w^2}$), as shown in Figs. 7b and 7c, respectively. The large TKE predicted by the UW model (open circle) is under-

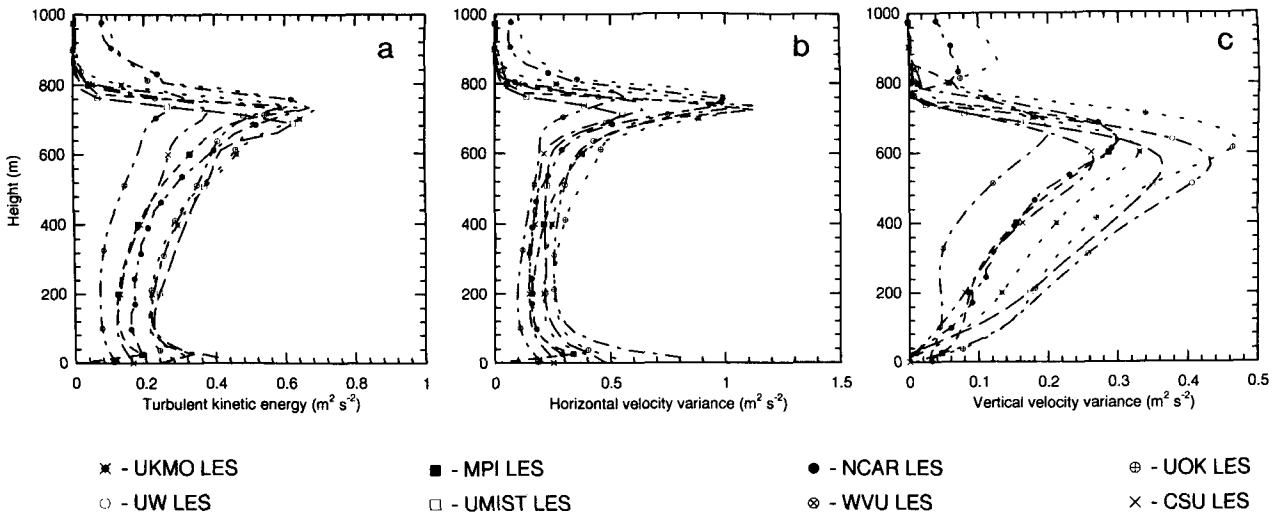

FIG. 7. Vertical profiles of (a) total TKE, (b) resolved-scale horizontal velocity variance, and (c) resolved-scale vertical velocity variance averaged over the second hour of simulation from the eight LES codes.

standable because the UW model also predicted the largest cloud-top cooling and, hence, the largest in-cloud buoyancy flux. Although KNMI did not supply their TKE data, based on their layer-averaged TKE shown in Fig. 3d, we expect to see large TKE from KNMI as well. This is consistent with the above argument. However, it is less clear why the UMIST (open square) and UOK (open plus circle) models also produced TKEs larger than in most LESs. (UKMO predicted a total TKE that is somewhat larger than in most LESs, but its resolved-scale horizontal and vertical velocity variances are about average. This implies that its subgrid-scale TKE, which is a purely diagnosed quantity in the Smagorinsky-type closures, is larger than in the others.) WVU, and possibly ARAP although the data are not available, predicted the smallest energy levels of all.

In this weak shear case, the major TKE source came from the buoyancy production, $g/T_0\ \overline{w\theta_v}$, shown in Fig. 8a, where $\overline{w\theta_v}$ is the buoyancy flux and g/T_0 is the buoyancy coefficient. The turbulent transport term, $-\partial\overline{wE}/\partial z$, is given in Fig. 8b, while the molecular dissipation is shown in Fig. 8c. Although the magnitudes differ somewhat among the simulations, the vertical shapes of these budget terms are quite similar.

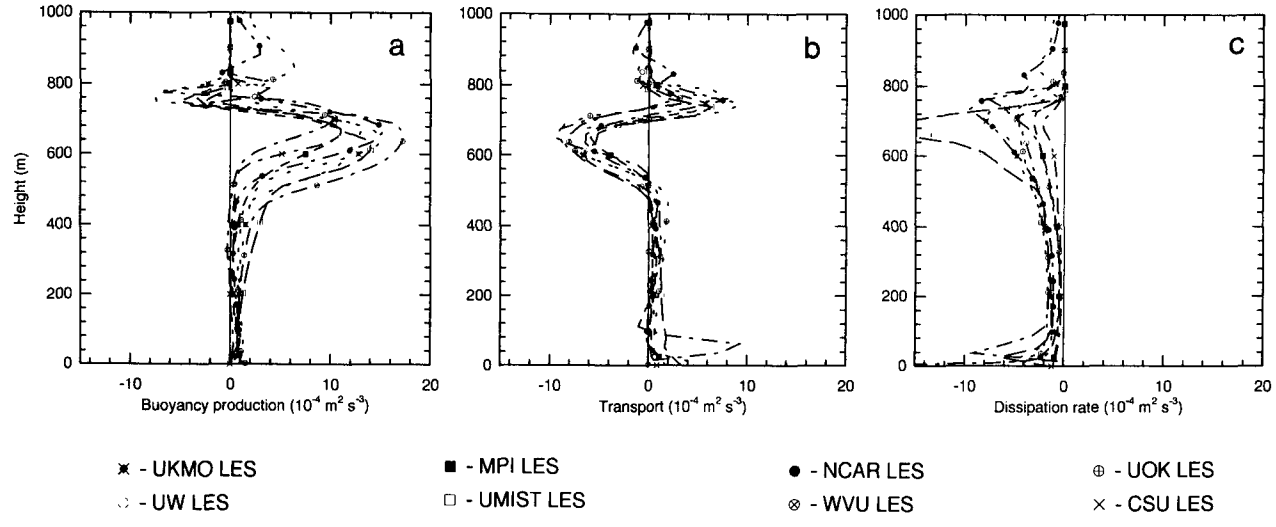

FIG. 8. Vertical profiles of the TKE budget terms averaged over the second hour of simulation from the eight LES codes: (a) buoyancy production, (b) turbulent transport, and (c) molecular dissipation.

b. The 2D CRM results

Figure 9 shows the IR heating rate from the four 2D CRMs averaged over the second hour. Again, the UW group gave the largest cloud-top IR cooling rate, consistent with its 3D LES result. All other three 2D CRMs predicted about the same amount of cloud-top IR cooling, although that maximum cooling occurred at different heights.

1) TIME EVOLUTION

The time evolution of the cloud-top height, cloud amount, LWP, and layer-averaged TKE from the four 2D CRMs are shown in Fig. 10. Most of these results are similar to the 3D simulation results, especially if we compare them only with their 3D counterparts (i.e., UKMO, UW, and CSU). Again, the UW simulation produced the largest amount of LWP, consistent with its 3D simulation.

One significant difference between the 2D and 3D results is the layer-averaged TKE level. The TKE from all 2D simulations is much higher, about 1 $m^2 s^{-2}$, compared to the average value of about 0.3 $m^2 s^{-2}$ from the 3D simulations. It is interesting, but puzzling, that in spite of the stronger TKE in the 2D simulations, the entrainment rate is rather similar to the 3D simulations. We suspect that the relationship between TKE and the entrainment rate is different between 2D and 3D turbulence.

2) VERTICAL DISTRIBUTIONS OF THE MEANS AND FLUXES

The mean temperature and moisture fields (Figs. 11a,b) from the 2D CRM simulations are very similar to those from the 3D simulations. Figure 11c shows that the variation of the liquid water mixing ratio among the 2D CRMs is similar to that among the 3D LESs. The UW-2D again predicted the largest liquid water mixing ratio, as the UW predicted the largest liquid water among all 3D LESs shown in Fig. 5c. Note also that both CSU-2D and UKMO-2D predicted about the same amount of liquid water peak value as did their 3D counterparts, which is about 0.2 g kg^{-1}.

Figure 12a shows the total (resolved plus subgrid-scale, except for UU-2D, which shows resolved only) momentum fluxes from the 2D CRMs except in the case of the UKMO-2D, since its model coordinate differed from the others such that its mean U is $(2^2 + 4^2)^{1/2} \sim 4.5$ m s^{-1} and V is zero, instead of 2 m s^{-1} and -4 m s^{-1}, respectively, as in the others. The y-component momentum fluxes from the 2D CRMs are similar to those from the 3D LESs. However, the x-component momentum fluxes from UU-2D and UW-2D are completely different from those of the 3D LESs. This is largely due to the significant eddy transport of horizontal momentum that occurs in the 2D

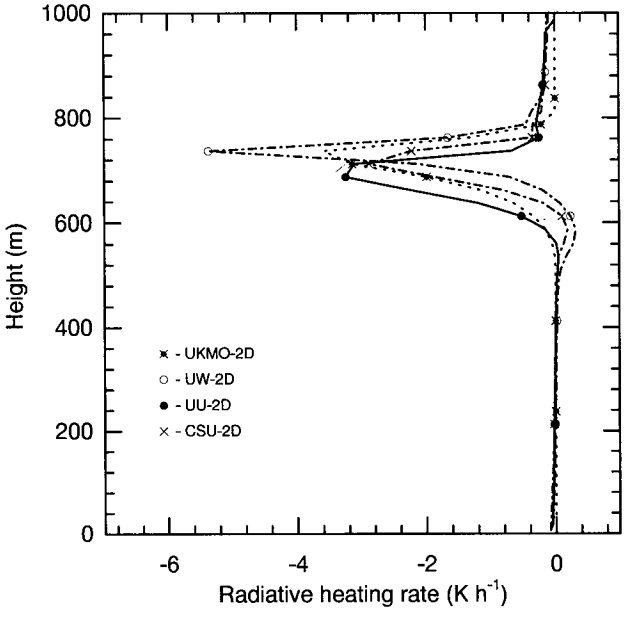

FIG. 9. Same as Fig. 2 except for the four 2D CRMs.

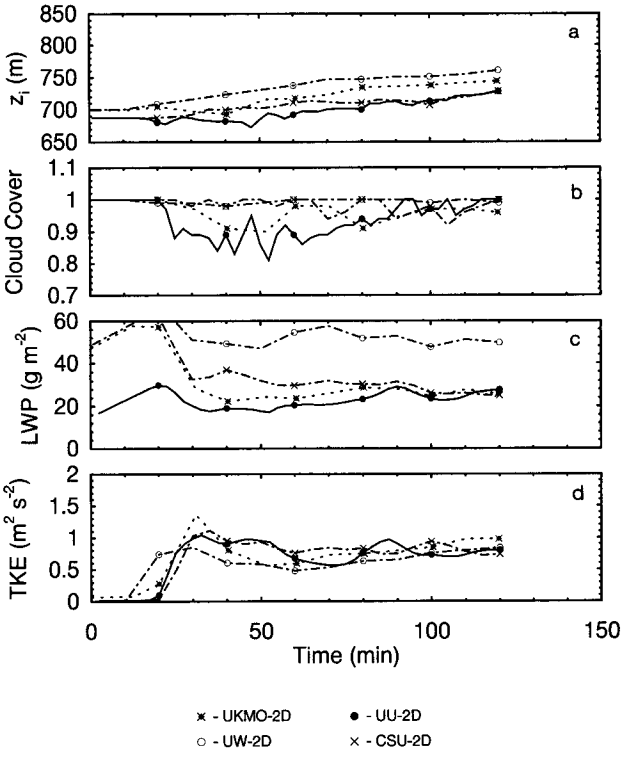

FIG. 10. Same as Fig. 3 except for the four 2D CRMS.

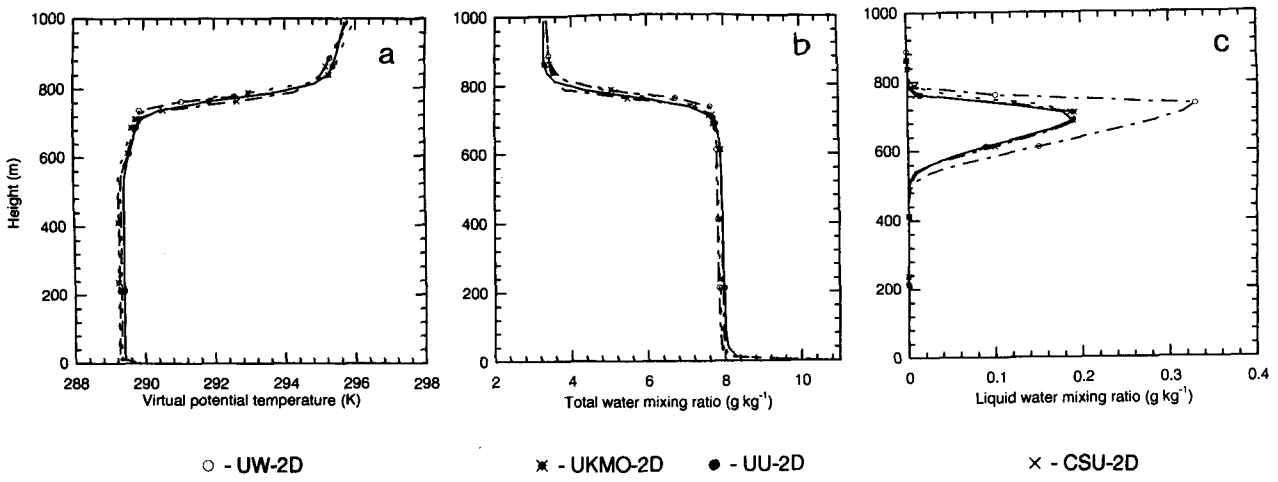

FIG. 11. Same as Fig. 5 except for the four 2D CRMs.

simulations as a result of the tilting of the convective rolls. And of course, part of the scatter is due to the data sampling problem.

The buoyancy and total water fluxes from 2D simulations (resolved plus subgrid-scale; Figs. 12b,c) show similar magnitudes and shapes to those of their 3D counterparts (i.e., UKMO, UW, and CSU).

3) VERTICAL PROFILES OF THE TKE AND ITS BUDGET

Among the statistics we compared, the most significant differences between 2D and 3D, besides the momentum flux profiles, are found in the kinetic energy level and the vertical distributions of the horizontal and vertical TKE components, as shown in Fig. 13. The total (resolved plus subgrid scale) TKE predicted from all 2D CRMs is about 0.7 m^2 s^{-2} in the mid-PBL, which is more than three times that from the average 3D LESs (about 0.2 m^2 s^{-2} in the mid-PBL). This difference shows up in both the resolved-scale horizontal (Fig. 13b) and vertical (Fig. 13c) components of TKE.

The profile shapes of the horizontal and vertical components of resolved-scale TKE from all 2D CRMS are significantly different from those of 3D LESs. Their horizontal TKE is less uniform in height in the mid-PBL than that of the 3D LESs, and their vertical TKE shows a maximum right in the middle of the PBL rather than in the upper cloud layer as in the 3D LESs. This reflects differences in detailed flow structures between 2D and 3D simulations. It is known that 2D simulations tend to produce large-scale horizontal roll circulations, while 3D simulations generate more chaotic plume motions.

The TKE partitioning is quite different in the UU-2D CRM prediction (solid curves) than in the other

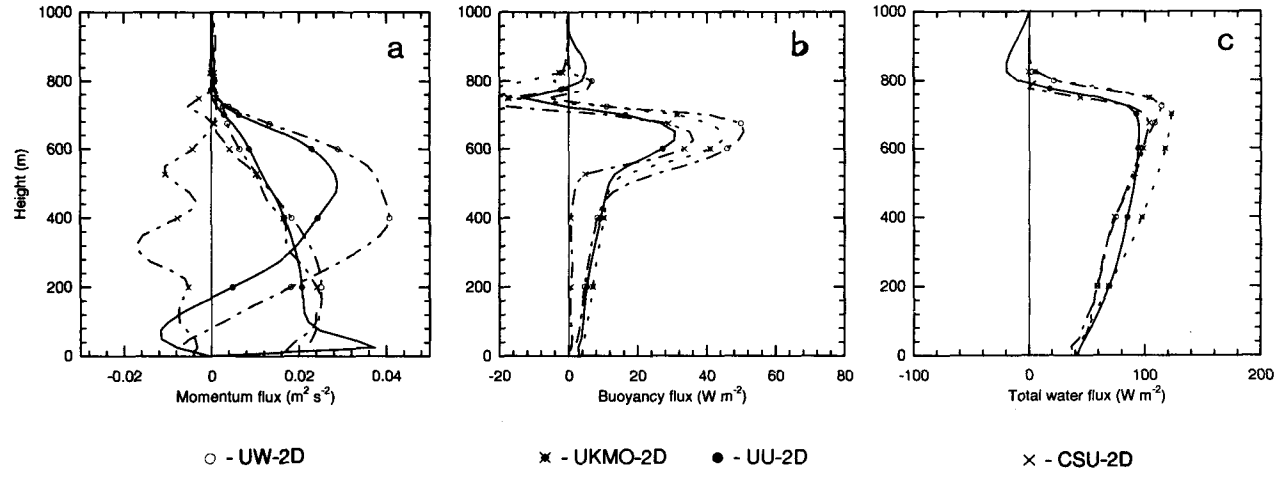

FIG. 12. Same as Fig. 6 except for the four 2D CRMs.

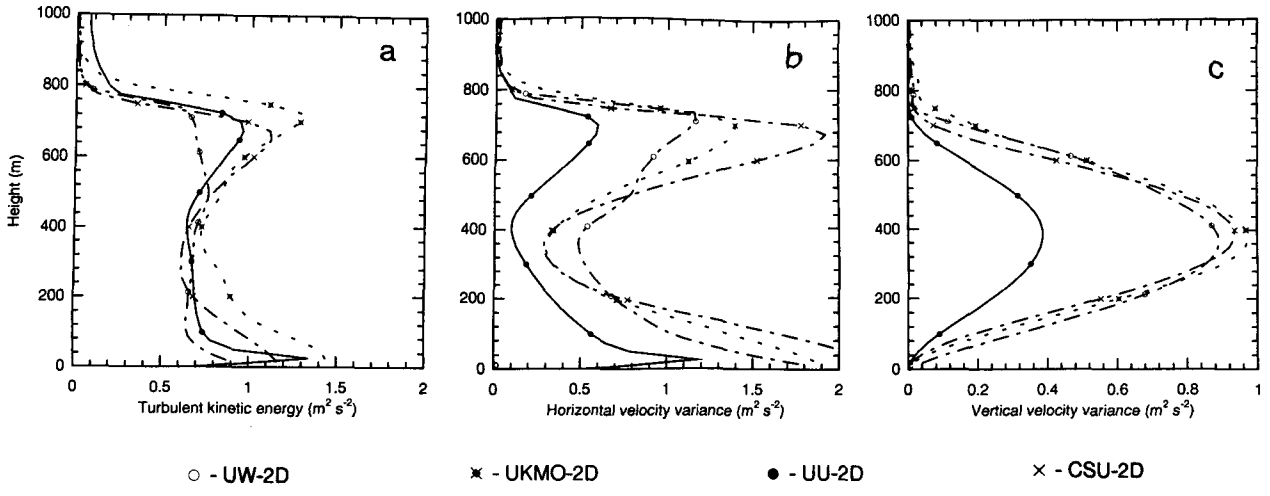

FIG. 13. Same as Fig. 7 except for the four 2D CRMs.

CRMs; it shows smaller resolved-scale horizontal and vertical TKE components than do the other 2D results. Since the UU-2D CRM's total TKE is about the same as the others', this implies that its unresolved TKE is larger than the others'. This is understandable because the UU-2D CRM uses an ensemble mean turbulence closure for its SGS turbulent motion, which is supposed to represent all turbulent motions except the resolved 2D motion. The other 2D CRMs used the Smagorinsky–Lilly type of turbulence scheme only for eddies smaller than the grid mesh, even though eddies that are larger than the grid mesh are 3D in nature and in principle are not "resolved" by a 2D simulation. Such a scheme is likely to generate a smaller "SGS" TKE, and hence allow for a stronger resolved-scale turbulent motion. Clearly, these two types of SGS turbulence schemes have different physical aspects.

The TKE budgets from three 2D CRMs (UU-2D data are not available) are given in Fig. 14. The prediction of the turbulent transport term (Fig. 14b) varied significantly among the 2D results, as did the dissipation predictions (Fig. 14c). For these higher-moment statistics, the variation among the 2D simulations is clearly larger than that among the 3D simulations.

5. Discussion and future work

Possible sources for the differences between the 10 LES solutions include the initial liquid water field; the numerics; the parameterizations of SGS turbulence, SGS condensation, and longwave radiation; and the saturation mixing ratio algorithm. We find that large differences occur in the cloud-top radiative cooling

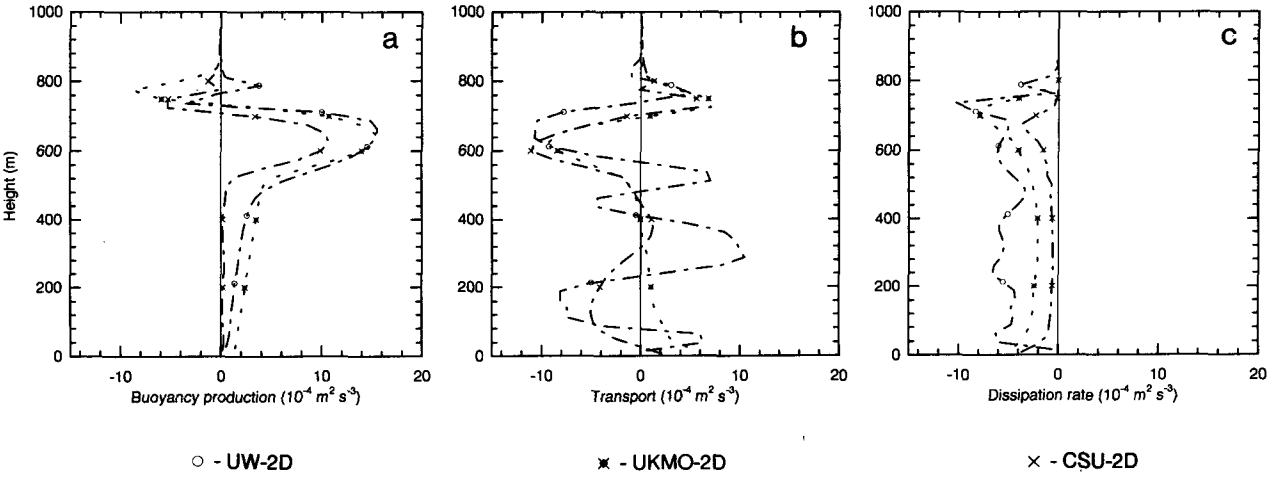

FIG. 14. Same as Fig. 8 except for the three 2D CRMs.

rate, which is internally determined in the simulations. For example, the KNMI and UW LESs predict the strongest cloud-top radiative cooling (Fig. 2) and, hence, produce the largest buoyancy fluxes (Fig. 6b).

From Figs. 2 and 3d, we plot the relationship between the maximum amount of cloud-top cooling rate (Q_{max}) and the layer-averaged TKE in Fig. 15a. To produce this plot, we divide the maximum cooling rate of the WVU LES by 2.5, since this code used a stretch vertical grid that has 10-m resolution near the cloud top while others used a uniform grid of 25 m. (Given the same amount of IR flux jump across the cloud top, a finer vertical grid near the cloud top yields a larger cooling rate.) Figure 15a shows some positive correlation between the cloud-top cooling and the layer-averaged TKE. If instead we plot the layer-averaged TKE against the net longwave radiative flux just above the maximum cooling level (F^{+}_{rad}), as shown in Fig. 15b, the correlation is better.

The algorithm for computing the saturation mixing ratio could be a significant source for the variation in the liquid water mixing ratio. A difference of only 2% in the calculated saturation mixing ratio can result in a ~25% difference in the peak value of the liquid water mixing ratio, because the liquid water mixing ratio is less than 10% of the saturation mixing ratio.

The large variation in the total water flux (Fig. 6c) is due mainly to the entrainment rate prediction; those models that predict the smallest entrainment rates (ARAP, WVU, and MPI) have the smallest total water fluxes. We also notice that these three models use the S–D condensation scheme, but we do not know if this is related to the prediction of the entrainment rate.

The entrainment rates vary significantly among the 10 LESs. We found that the entrainment rate seems to correlate well with the layer-averaged TKE (Fig. 16a, where dz_i/dt is from Table 4) and, hence, is correlated somewhat with the above-cloud-top radiative flux (Fig. 16b). As mentioned above, the large variation of the entrainment rates could be due to the different treatments of numerics (or more specifically, the vertical advection), SGS turbulence, radiation, and SGS condensation. To focus on the entrainment rate issue, the workshop participants recommended an immediate follow-up experiment: a smoke-cloud simulation, in which the latent heating effect is to be excluded, thus eliminating any variations due to different SGS condensation schemes or saturation mixing ratio algorithms. In addition, all LESs will use the same longwave radiation formula in order to reduce differences in cloud-top forcing. From this follow-up experiment, we hope to see whether LESs can provide a consistent prediction of the entrainment rate.

The problem of not having sufficiently accurate entrainment rate observations for the verification of LES was also discussed in the workshop. D. Lenschow proposed two methods for more accurate aircraft measurements of the entrainment rate. One of these is the measurement of vertical flux profiles of a tracer through the boundary layer and the jump in the species concentration across the PBL top. A particularly attractive trace species is the dimethyl sulfide (DMS) eddy flux, which is emitted by phytoplankton in the ocean and has a lifetime of a day or so in the atmosphere. Thus, the DMS concentration above the PBL is small, and its jump value across the PBL top is easy to detect. This jump condition, along with an estimate of the DMS flux at the cloud top, can provide an estimate of the entrainment rate, since the entrainment rate is the negative of the ratio of the flux to the jump value across the top. The second method proposed by Lenschow involves obtaining more accurate measurements of the lateral component of the wind with respect to the aircraft around closed horizontal flight paths from which large-scale divergence can be mea-

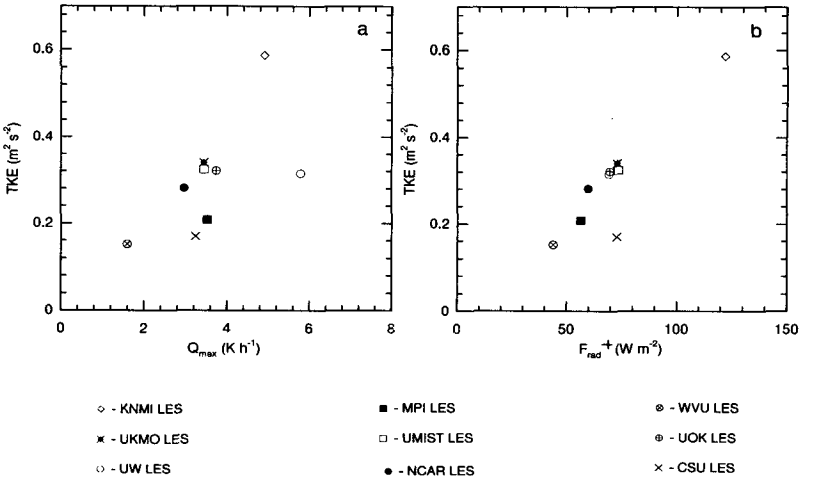

FIG. 15. Correlation plots of layer-averaged TKE vs (a) maximum cloud-top IR cooling rate and (b) the IR flux just above the maximum IR cooling level among the LES simulations averaged over the second hour period.

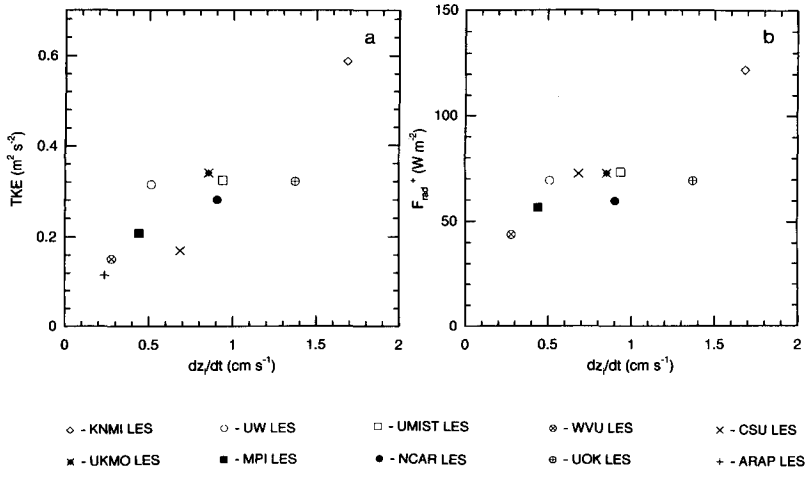

FIG. 16. Correlation plots of the growth rate of the cloud-top height vs (a) layer-averaged TKE and (b) the IR flux just above the maximum IR cooling level from the 10 LES simulations averaged over the second hour period.

sured. The large-scale (mean) vertical motion at cloud top can then be estimated from the vertical integral of the divergence obtained at several levels through the PBL. The difference between the mean vertical motion at cloud top and the cloud growth rate yields an independent estimate of the entrainment rate. Both of these entrainment rate estimates can be obtained simultaneously from a single aircraft.

The comparisons between 2D CRM simulations and 3D LESs suggest that 2D CRM simulations are useful for studying the overall evolution of the mean and scalar flux profiles within the radiatively driven stratocumulus-topped PBL despite the obvious differences between eddy structure in 2D and 3D. However, the momentum fluxes, the vertical and horizontal velocity variances, the TKE, and the TKE budget terms all differ significantly from those of the 3D LESs.

This first intercomparison workshop has also proven to be useful in identifying errors that existed in some model codes and in the analysis of statistics. Plans are to hold a second GCSS Boundary Layer Cloud Workshop at KNMI in the Netherlands from 30 August to 1 September 1995. This workshop will focus on the smoke-topped PBL case as well as two ASTEX (Atlantic Stratocumulus Transition Experiment) Lagrangian cases. Since to date there exists no measurement of the entrainment rate that is sufficiently accurate to verify LES results, the smoke cloud simulation provides the simplest case for studying entrainment. The ASTEX cases include drizzle in one and solar radiative heating and a cumulus-under-stratocumulus cloud regime in the other. These are fairly complex cases whose main advantage is that some cloud and turbulence properties were reported by Bretherton and Pincus (1995), Bretherton et al. (1995), and Duynkerke et al. (1995), which can be used for verification of LES. These two cases will be our first attempt to simulate observations. Results from this workshop will be reported in future articles.

Acknowledgments. W. R. Cotton's research was funded by the U.S. Department of Energy's National Institute for Global Environmental Change (NIGEC) at Tulane University (Cooperative Agreement DE-FC0390ER61010). S. Krueger's research was supported by the Office of Naval Research (ONR) Grant N00014-91-J-1175. The WVU participation was funded by ONR Grant N00014-93-1-0395. We thank Don Lenschow for his input on the entrainment rate measurements.

Appendix A: Model abbreviations and references

ARAP	3D LES of the Aeronautical Research Associates of Princeton, Inc. (Sykes and Henn 1989)
CSU	3D LES of the Colorado State University (Pielke et al. 1992)
CSU-2D	2D CRM of the Colorado State University (Pielke et al. 1992)
KNMI	3D LES of the Royal Netherlands Meteorological Institute, the Netherlands (Cuijpers and Duynkerke 1993)
MPI	3D LES of the Max-Planck-Institut für Meteorologie, Germany (Chlond 1992)
NCAR	3D LES of the National Center for Atmospheric Research (Moeng 1986)
UKMO	3D LES of the Meteorological Office, United Kingdom (Shutts and Gray 1994)
UKMO-2D	2D CRM of the Meteorological Office, United Kingdom (Shutts and Gray 1994)
UMIST	3D LES of the University of Manchester Institute of Science and Technology (Mason 1989)
UOK	3D LES of the University of Oklahoma
UU-2D	2D CRM of the University of Utah (Krueger et al. 1995)

UW	3D LES of the University of Washington (Rand 1995)
UW-2D	2D CRM of the University of Washington (Rand 1995)
WVU	3D LES of the West Virginia University (Sykes et al. 1990)

Appendix B: Initial sounding

The following Fortran code can be used to generate the initial sounding. Given a height z, this code will produce the dry potential temperature θ and total water mixing ratio q_T for the initial sounding. Note that the sounding produced by this code has the liquid water potential temperature decreasing with height within the cloud layer, which is unstable to moist convection:

```
TSLOPE1 = (288.32–288.00)/(690.–0.)
TSLOPE2 = (294.40–288.32)/(785.–690.)
TSLOPE3 = (295.30–294.40)/(1000.–785.)
TSLOPE4 = (299.40–295.30)/(2000.–1000.)
QSLOPE2 = 1.E-3 (3.50–8.10)/(785.–690.)
QSLOPE3 = 1.E-3 (3.37–3.50)/(1000.–785.)
QSLOPE4 = 1.E-3 (2.81–3.37)/(2000.–1000.)
if (z.LE.690.) then
θ = 288.00 + (TSLOPE1)z
q_T = 8.10E-3
elseif (z.le.785.) then
θ = 288.32 + (TSLOPE2)(z–690.)
q_T = 8.10E-3 + (QSLOPE2)(z–690.)
elseif (z.le.1000.) then
θ = 294.40 + (TSLOPE3)(z–785.)
q_T = 3.50E-3 + (QSLOPE3)(z–785.)
elseif (z.le.2000.) then
θ = 295.30 + (TSLOPE4)(z–1000.)
q_T = 3.37E-3 + (QSLOPE4)(z–1000.)
endif
```

References

Andren, A., A. R. Brown, J. Graf, P. J. Mason, C.-H. Moeng, F. T. M. Nieuwstadt, and U. Schumann, 1994: Large-eddy simulation of a neutrally stratified boundary layer: A comparison of four computer codes. *Quart. J. Roy. Meteor. Soc.*, **120,** 1457–1484.

Betts, A. K., and R. Boers, 1990: A cloudiness transition in a marine boundary layer. *J. Atmos. Sci.*, **47,** 1480–1497.

Bretherton, C. S., and R. Pincus, 1995: Cloudiness and marine boundary layer dynamics in the ASTEX Lagrangian experiments. Part I: Synoptic setting and vertical structure. *J. Atmos. Sci.*, **52,** 2707–2723.

——, P. Austin, and S. T. Siems, 1995: Cloudiness and marine boundary layer dynamics in the ASTEX Lagrangian experiments. Part II: Cloudiness, drizzle, surface fluxes, and entrainment. *J. Atmos. Sci.*, **52,** 2724–2735.

Browning, K. A., 1993: The GEWEX Cloud System Study (GCSS). *Bull. Amer. Meteor. Soc.*, **74,** 387–399.

Chlond, A., 1992: Three-dimensional simulation of cloud street development during a cold air outbreak. *Bound.-Layer Meteor.*, **38,** 161–200.

Cuijpers, J. W. M., and P. G. Duynkerke, 1993: Large eddy simulation of trade-wind cumulus clouds. *J. Atmos. Sci.*, **50,** 3894–3908.

Deardorff, J. W., 1980a: Stratocumulus-capped mixed layers derived from a three-dimensional model. *Bound.-Layer Meteor.*, **18,** 495–527.

——, 1980b: Cloud-top entrainment instability. *J. Atmos. Sci.*, **37,** 131–147.

Duda, D. P., G. L. Stephens, and S. K. Cox, 1991: Microphysical and radiative properties of marine stratocumulus from tethered balloon measurements. *J. Appl. Meteor.*, **30,** 170–186.

Duynkerke, P. G., H. Zhang, and P. J. Jonker, 1995: Microphysical and turbulent structure of nocturnal stratocumulus as observed during ASTEX. *J. Atmos. Sci.*, **52,** 2763–2777.

Krueger, S. K., G. T. McLean, and Q. Fu, 1995: Numerical simulation of the stratus-to-cumulus transition in the subtropical marine boundary layer. Part I: Boundary-layer structure. *J. Atmos. Sci.*, **52,** 2839–2850.

Kuo, H., and W. H. Schubert, 1988: Stability of cloud-topped boundary layer. *Quart. J. Roy. Meteor. Soc.*, **114,** 887–917.

Lenschow, D. H., and B. B. Stankov, 1986: Length scales in the convective boundary layer. *J. Atmos. Sci.*, **43,** 1198–1209.

Lilly, D. K., 1967: The representation of small-scale turbulence in numerical simulation experiments. *Proc. IBM Scientific Computing Symp. on Environmental Science*, Yorktown Heights, NY, 195–210.

MacVean, M. K., and P. J. Mason, 1990: Cloud-top entrainment instability through small-scale mixing and its parameterization in numerical models. *J. Atmos. Sci.*, **47,** 1012–1030.

Mason, P. J., 1989: Large eddy simulations of the convective atmospheric boundary layer. *J. Atmos. Sci.*, **46,** 1492–1516.

——, and N. S. Callen, 1986: On the magnitude of the subgrid-scale eddy coefficient in large-eddy simulations of turbulent channel flow. *J. Fluid Mech.*, **162,** 439–462.

Moeng, C.-H., 1986: Large-eddy simulation of a stratus-topped boundary layer. *J. Atmos. Sci.*, **43,** 2886–2900.

——, and J. C. Wyngaard, 1988: Spectral analysis of large-eddy simulations of the convective boundary layer. *J. Atmos. Sci.*, **45,** 3573–3587.

Nieuwstadt, F. T. M., P. J. Mason, C.-H. Moeng, and U. Schumann, 1992: Large-eddy simulation of the convective boundary layer: A comparison of four computer codes. *Turbulent Shear Flows 8,* F. Durst et al., Eds., Springer-Verlag, 343–367.

Pielke, R. A., and Coauthors, 1992: A comprehensive meteorological modeling system—RAMS. *Meteor. Atmos. Phys.*, **49,** 69–91.

Rand, H. A., 1995: Mesoscale dynamics of the marine atmospheric boundary layer. Ph.D. thesis, University of Washington, 134 pp.

Randall, D. A., 1980: Conditional instability of the first kind upside-down. *J. Atmos. Sci.*, **37,** 125–130.

Shutts, G. J., and M. E. B. Gray, 1994: A numerical modelling study of the geostrophic adjustment process following deep convection. *Quart. J. Roy. Meteor. Soc.*, **120,** 1145–1178.

Siems, S. T., C. S. Bretherton, M. B. Baker, S. S. Shy, and R. E. Breidenthal, 1990: Buoyancy reversal and cloud-top entrainment instability. *Quart. J. Roy. Meteor. Soc.*, **116,** 705–739.

Smagorinsky, J., 1963: General circulation experiments with the primitive equations. *Mon. Wea. Rev.*, **91,** 99–165.

Sommeria, G., and J. W. Deardorff, 1977: Subgrid-scale condensation in models of nonprecipitating clouds. *J. Atmos. Sci.*, **34,** 344–355.

Sykes, R. I., and D. S. Henn, 1989: Large-eddy simulation of turbulent sheared convection. *J. Atmos. Sci.*, **46,** 1106–1118.

——, W. S. Lewellen, and D. S. Henn, 1990: Numerical simulation of the boundary-layer eddy structure during the cold-air outbreak of GALE IOP 2. *Mon. Wea. Rev.*, **118,** 363–373.